Title

Highly Active Rutile TiO2 Nanocrystalline Photocatalysts

Journal

ACS Applied Materials & Interfaces, 12(29)

ISSN

1944-8244

Authors

Djokić, Veljko R

Marinković, Aleksandar D

Petrović, Rada D

et al.

Publication Date

2020-07-22

DOI

10.1021/acsami.0c03150

Peer reviewed

Highly active rutile TiO_2 nanocrystalline photocatalysts

Veljko R. Djokić[a,], Aleksandar D. Marinković[a], Rada D. Petrović[a], Ovidiu Ersen[b], Spyridon Zafeiratos[c], Miodrag Mitrić[d], Colin Ophus[e], Velimir R. Radmilović[a,f,]* and Djordje T. Janaćković[a,]**

[a] Faculty of Technology and Metallurgy, University of Belgrade, Karnegijeva 4, 11120 Belgrade, Serbia

[b] Institut de Physique et Chimie des Matériaux de Strasbourg (IPCMS), UMR CNRS – Université de Strasbourg 7504, 23, rue du Loess, BP 43, F-67034 Strasbourg Cedex 2, France

[c] Institut de Chimie et Procédés pour l'Energie, l'Environnement et la Sante (ICPEES), ECPM, UMR 7515 du CNRS, Strasbourg University, 25 rue Becquerel, 67087 Strasbourg Cedex 02, France

[d] Condensed Matter Physics Laboratory, Vinča Institute, University of Belgrade, P. O. Box 522, 11001 Belgrade, Serbia

[e] NCEM, Molecular Foundry, Lawrence Berkeley National Laboratory, Berkeley, CA, USA 94720

[f] Serbian Academy of Sciences and Arts, Knez Mihailova 35, 11000 Belgrade, Serbia

ABSTRACT: The controllable synthesis of rutile TiO_2 single crystal particles with preferential orientation of {111} facets still remain a scientific and technological challenge. Here, we developed a facile route to fabrication of rutile TiO_2 nanorod crystals ($RTiO_2NRs$) having high ratios of oxidative {111} to reductive {110} surfaces. $RTiO_2NRs$ were synthesized using a peroxo-titanium complex (PTC) approach, which was controlled by changing the Ti/H_2O_2 ratio. The thus obtained $RTiO_2NRs$ revealed a high tendency to agglomerate through orientation-dependent attachment along the {110} facets. This resulted in an increased {111}/{110} surface ratio and lead to a markedly improved photocatalytic activity of $RTiO_2NRs$ aggregates. The reported findings illustrate the rich potential of the herein proposed facile and energy-efficient synthesis of nanostructured rutile TiO_2-based photocatalysts.

KEYWORDS: TiO_2, Rutile nanorods, Photocatalysis, Orientation-dependent attachment, Self-assembly.

INTRODUCTION

Titanium dioxide (TiO_2) is one of the most widely studied semiconductors (*n*-type) due to its low cost, abundant resource, high photocatalytic activity, resistance to chemical corrosion and photo-corrosion and non-toxicity.[1] Since the discovery of the photo-induced decomposition of water on TiO_2 electrodes,[2] interest in TiO_2 as a strategic material for environmental protection and photo-electrochemical solar energy conversion has continuously increased. These applications are mainly related to photocatalysis, artificial photosynthesis, dye-sensitized and metal halide perovskite solar cells, anti-fogging and self-cleaning surfaces, sterilization, agriculture, sensors, paintings, as well as potential drugs in cancer treatment.[1,38,9,10,11,12] Under

ambient conditions, TiO_2 can exist in eight crystalline polymorphs, of which only three, *i.e.* rutile (tetragonal), anatase (tetragonal) and brookite (orthorhombic), are naturally occurring.[13,14] Each of the TiO_2 polymorphs exhibits specific physical properties, such as the band gap, surface states, defect sites density, photocatalytic activity, *etc*.[15,16] Phase-controlled synthesis of anatase and rutile depends on several factors, including solution pH, reactant concentration and the employed mineralizer.[3-7,16] Most rutile photocatalysts show lower photocatalytic activity than anatase photocatalyts,[16-18] although nanostructured rutile TiO_2 could exhibit advantageous properties compared to anatase, including higher absorption in the visible light region and better chemical stability.[19] Under certain circumstances the above-mentioned features of rutile may result in its higher photocatalytic activity.[20]

A wide variety of methods have been used to synthesize rutile TiO_2 nanoparticles with favorable photocatalytic properties. In particular, quite a number of studies[17-18,21-24] describe synthesis routes based on implementing peroxo-titanium complexes (PTC). In this approach PTC may be obtained from various types of TiO_2 precursors and hydrogen peroxide (H_2O_2). It was emphasized that the obtained crystallite size was significantly lower starting from titania alkoxide precursors, and only moderate photocatalytic activities of the obtained materials were reported.[17,21]

In order to evaluate and explain properly the photocatalytic activity of nanocrystalline materials, it is important to study nanocrystal growth and morphological evolution (surface area, porosity, the presence of surface facets, *etc.*), because they affect the intensity of interaction

between ions or molecules and nanocrystal free surfaces (surface facets). Morphology evolution is of particular importance because it may significantly modify physical properties and surface reactivity.[25] It was recently demonstrated that the catalytic activity of TiO_2 nanocrystals depended on the average particle size and type of oxygen donor, namely O_2 or H_2O_2, and when the oxygen donor was H_2O_2, rutile crystals showed the highest activity.[26,27] It was also speculated that the origin of this phenomena was the slow recombination rate of the electron–hole pair in rutile when the oxidant was H_2O_2. Some other authors suggest the opposite idea, that the inferior photocatalytic activity of rutile TiO_2 nanoparticles could be correlated with the intrinsic recombination of photogenerated electron–hole pairs.[28] Banfield et al. discovered that nanocrystal morphology could change under hydrothermal conditions through the attachment of crystallographically oriented individual particles.[25,29] It was also shown that anisotropic growth of a rutile nanocrystal along the [001] direction produced a nanorod with dominantly exposed reductive {110} lateral facets and oxidative {111} top-facets.[30,31] The latter facets are thermodynamically less stable, and usually represent a small fraction of the TiO_2 nanorod surface.[32] Therefore, enhancement of photocatalysis, *i.e.*, efficient electron/hole separation at reductive/oxidative exposed facets, was achieved by increasing the surface area ratio of oxidative to reductive crystal facets.[30,33,34]

The aim of this research was to study the effect of the Ti/H_2O_2 molar ratio and the decomposition time of the peroxo-titanium complex (PTC) on the crystal structure, crystallite size and nanoscale morphology evolution of rutile TiO_2 nanorod crystals ($RTiO_2NRs$), as well as to elucidate the effect of self-aggregation of $RTiO_2NRs$ on their photocatalytic activity.

RTiO$_2$NRs photocatalysts synthesized with using three different Ti/H$_2$O$_2$ molar ratios, *i.e.* of 1/100, 1/110 and 1/150, are hereinafter referred to as PTA 1/100, PTA 1/110 and PTA 1/150.

RESULTS AND DISCUSSION

Most of the results presented here are for the PTA 1/100 molar ratio sample, corresponding to 48 hours of PTC decomposition, as this sample revealed the highest photocatalytic activity.

The details of the experimental approach related to the synthesis and entire preparation procedure implemented to obtain reproducible and size-controlled PTA aggregates, methods used for characterization, and the photocatalytic study of the PTA catalysts are given in the experimental section.

FTIR analysis of the synthesized RTiO$_2$NRs was performed to estimate qualitatively the presence of residual functional groups at the nanorod surface. The FTIR spectra of PTA nanorods, prepared with using Ti/H$_2$O$_2$ molar ratios of 1/100, 1/110 and 1/150, are shown in Fig. 1. The corresponding FTIR spectra collected for the PTA 1/100 sample, prepared using different PTC decomposition times, are depicted in Fig. S1.

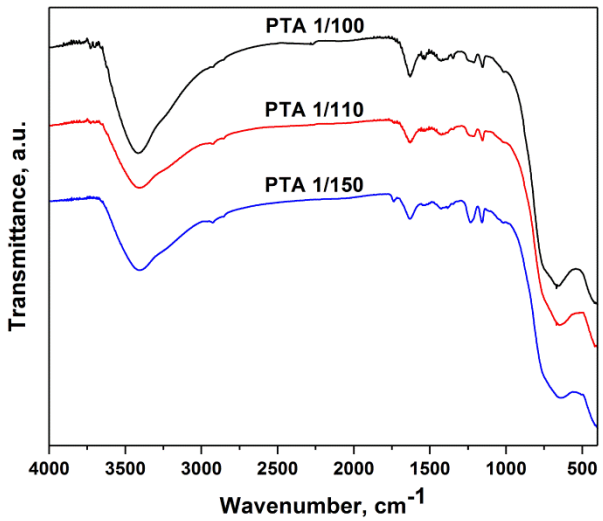

Figure 1. FTIR spectra of PTA nanorods obtained using three different Ti/H_2O_2 molar ratios: 1/100 (black trace), 1/110 (red trace), and 1/150 (blue trace).

As can be seen in Fig. 1, all three materials of the dried PTA nanorods exhibited peaks at 570, 1120, 1220, 1404 and 1630 cm^{-1}, as well as a broad band at 3200–3600 cm^{-1}. The absorptions with maxima at ~3400 cm^{-1} and 1630 cm^{-1} can be assigned to the stretching and bending vibrations of OH groups, respectively, present at the TiO_2 surface and from adsorbed water. The stretching vibration of the peroxo bond (–O–O–) of TiO_2 sol, observed at ~900 cm^{-1}, disappeared after 16 h of thermal treatment, as recently reported in the literature.[22] The broad adsorption due to the stretching vibrations of Ti–OH bond was observed at ≈ 570 cm^{-1}. The peaks at 1350 and 1550 cm^{-1} represent $\nu_{sym}(COO^-)$ and $\nu_{asym}(COO^-)$, respectively. The difference between the *sym* (symmetric) and *asym* (asymmetric) vibrations is around 200 cm^{-1}, which indicates that carboxylates groups are bound to Ti(IV) in a monodentate manner. It was shown that the formate anion, HCO_2^-, could coordinate in both manners, *i.e.* monodentate or bidentate, while preferentially bridging two Ti sites on the {110} surface due to the greater distance between Ti sites at the {111} surface.[35] Analogously, the propionate could create a bridging coordination complex, and they could contribute to oriented attachment between rutile nanorods. The peaks at 1120 and 1220 cm^{-1} could be assigned to *sym* and *asym* vibrations of the C–O bond of the surface-attached propionate moieties.

The pure crystallized and shape-controlled rutile nanoparticles were further analyzed by the XRD technique. The synthesized TiO_2 catalysts at different molar ratios after decomposition of 48 h (Fig. 2), and different decomposition times at a 1/100 molar ratio (Fig. S2) showed XRD patterns attributed to the pure rutile phase (tetragonal space group $P4_2/mnm$ (D_{4h}, No. 136) with

the lattice parameters a=b=0.452 nm and c=0.294 nm). These patterns exhibited the strong characteristic peaks at 2θ = 27.5°, 36.1° and 54.4° that correspond to the rutile planes (110), (101) and (211), respectively. Additionally, the (111) reflection in the XRD patterns (Fig. 2), appears to have higher intensity in comparison to the standard rutile diffraction patterns, and recently published results.[30]

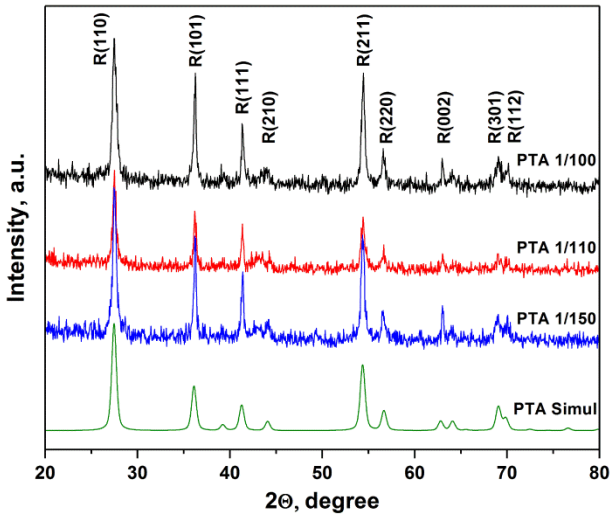

Figure 2. Powder XRD patterns collected for the synthesized PTA nanorods, PTA 1/100 (black trace), PTA 1/110 (red trace), PTA 1/150 (blue trace), and simulated XRD pattern of rutile TiO_2 with a random crystallite orientation, PTA Simul (green trace).

The diffraction intensity ratios ($I_{(110)}/I_{(101)}$) and ($I_{(111)}/I_{(101)}$), given in Table 1, indicates the presence of aggregates with preferentially orientated {111} facets. The highest diffraction intensity ratio $I_{(111)}/I_{(101)}$ of well-crystallized nanorods PTA 1/100 is clear indication of the importance of oxidative {111} facets for enhanced photocatalytic activity (discussed below).

Table 1. Diffraction intensity ratios of the (110) to (101) ($I_{(110)}/I_{(101)}$) and (111) to (101) ($I_{(111)}/I_{(101)}$) XRD peaks for the synthesized PTA nanorods.

Rutile TiO_2	$I_{(110)}/I_{(101)}$	$I_{(111)}/I_{(101)}$
PTA 1/100[a]	1.25	0.59
PTA 1/100[b]	1.27	0.61
PTA 1/110	1.61	0.58
PTA 1/150	1.41	0.56
Ref.[30]	1.98	0.44
Ref.[36]	0.41	0.31

[a] – transmission mode; [b] – reflection mode

The evolution of the nanocrystals was analyzed by TEM and XRD, and it was found that Ti/H_2O_2 molar ratio was the main factor controlling the crystal size and morphology. Increasing the Ti/H_2O_2 ratio did not induce the formation of a different crystal structure, while the peak width decreased, indicating crystal growth. The mean crystallite diameter of the primary nanoparticles, determined using the Scherrer formula, were 13±0.4, 14±0.5 and 17±0.6 nm, obtained at 1/100, 1/110 and 1/150 Ti/H_2O_2 ratio, respectively. Small influences of the PTA decomposition time on the crystallite size could be noticed from Table S1.

The textural parameters of the synthesized titania powders are given in Tables 2 and S2, while the pore size distributions of the PTA 1/100 and PTA 1/150 nanorods are shown in Fig. S3, from which it could be observed that the powders had a broad mesopore size distribution in relation to the pores in the clusters.

Table 2. Textural parameters of the PTA 1/100, PTA 1/110 and PTA 1/150 nanorods

Parameter/ PTA nanorods	PTA 1/100	PTA 1/110	PTA 1/150
Specific surface area, S_{BET} (m^2 g^{-1})	72.439 (±0.763)	68.105 (±0.150)	65.386 (±0.161)
Total pore volume, V_{total} (cm^3 g^{-1})	0.378	0.367	0.329
Mesopore volume, V_{meso} (cm^3 g^{-1})	0.369	0.362	0.315
Mean mesopore diameter D_{mean} (nm)	23.477	24.426	26.909

The specific surface area, total pore and mesopore volumes decreases as the Ti/H_2O_2 ratio and decomposition time increases (Tables 2 and S2). Such findings are an indication that the crystallite size and interparticle voids at the higher Ti/H_2O_2 molar ratio increased as a result of either nanoparticles coarsening or nucleation and crystal growth inside the mesopores.[37,38] The correlation of BET (Brunauer-Emmett-Teller) analysis (Tables 2 and S2) with the photocatalytic studies (presented later in the text), indicates an influence of the textural parameters on the photocatalytic performance, which means that the availability of surface active sites is of significance to enhance photocatalysis.

The light-absorbing properties of the synthesized photocatalysts were characterized by diffuse reflectance spectroscopy (DRS). The corresponding UV-VIS absorbance spectra deduced from DRS measurements for PTA 1/100 nanorods synthesized using various PTC decomposition times are shown in Fig. 3a. The values of the absorption edges of the photocatalysts are associated with the point of intersection of the tangent line to the plotted curve inflection point with the horizontal (zero line) axis (Fig. 3a and Table S3).

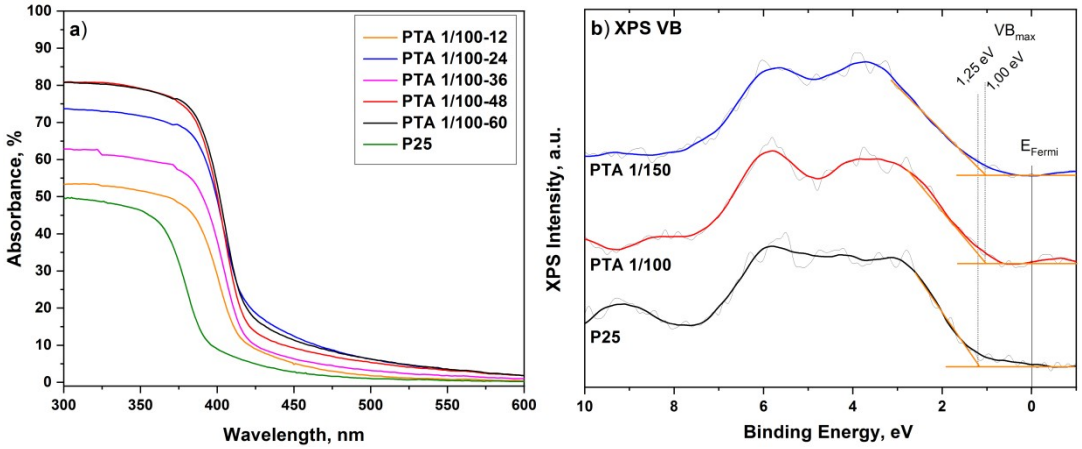

Figure 3. **a**) UV-VIS absorbance spectra (deduced from DRS measurements) collected for PTA 1/100 nanorods synthesized using various PTC decomposition times (in the range from 12 to 60 h) and for TiO_2 P25 reference material; b) Valence band (VB) XPS spectra of two selected PTA nanorods, PTA 1/100 and PTA 1/150, as well as of TiO_2 P25 reference material.

The band gaps corresponding to these absorption edges were calculated according to the reported procedure.[39] The average value of the deduced band gaps was 2.94 eV, with the standard deviation (STD) of 0.01 eV. The details are presented in Table S3.

Form Figure 3a is evident that PTA 1/100 nanorods have a stronger absorption in the UV-visible range and are red-shifted in the band gap transition, as compared to P25. This finding can be explained by the well-known differences in the optical absorption edges of the various TiO_2 phases. In particular, the adsorption edge of the pure rutile phase is red-shifted of about 25 nm as compared to the anatase TiO_2.[37,40,41]. Since PTA 1/100 samples are composed of pure rutile TiO_2 phase, the corresponding UV-Vis absorption edge are red-shifted compared to P25 which is a mixed anatase/rutile phase with a ratio of about 5.[42] . Additionally, the observed small narrowing of the band gap of PTA 1/100 (Figure 3a), by about 0.06 eV relative to pure rutile (*Eg*=3.0 eV),

could be explained by the presence of edge dislocations (see Figure 6) that reduce the band gap by modification of conduction band energy, due to the applied strain.[43,44] Thus, the more advantageous electronic structure of the synthesized photocatalysts, due to lower band gap values than for P25, significantly contributed to an efficient electron-hole excitation**.**

This is also confirmed in the photoemission spectra of the valence band (VB) recorded by AlKa radiation and shown in Fig. 3b. The intense features located between 1.5 eV and 8 eV binding energies are assigned to O 2p–Ti 3d hybridized states, as has been previously discussed.[45] The valance band maxima can be calculated from these spectra by linearly extrapolating the peaks to the base lines. The location of the VB maximum between PTA and reference P25 sample shows some small but systematic differences. In particular, the VBmax of PTA samples shifts about 0.25 eV towards the Fermi level as compared to P25 sample. This is in agreement with previous work which showed that the VBmax of oxygen rich TiO_2 shifts to lower binding energies, *i.e.* towards the Fermi edge.[46]

The morphology of the synthesized photocatalysts was analyzed from FEG–SEM and TEM/HRTEM results. Based on the FEG–SEM analysis (Fig. S4), the dimensions of nanorods, determined using MIRA TESCAN *in situ* measurement software, were: length 142±13 nm and width 34±4 nm for TiO_2 nanorods obtained at a 1/100 Ti/H_2O_2 ratio, while larger rode-like clusters of 217±17 nm length and 50±6 nm width were obtained at a 1/150 Ti/H_2O_2 molar ratio. The particle size distributions of all samples were narrow. We observe that generally as the Ti/H_2O_2 molar ratio is increased, both nucleation and crystal growth occur more quickly, resulting in larger primary crystallites, as shown by XRD results. These larger crystallites then linked into

much larger aggregates, by orientation-dependent attachment along the {110} facets (these processes will be explained in detail later in the text).

The TEM images in Figs. 4 and S5 show morphology typical for $RTiO_2NR$ clusters. The time-dependent PTC decomposition for a 1/100 Ti/H_2O_2 molar ratio (Fig. S6) shows the evolution of the nanorod morphology and the formation of more defined cluster of nanorods with increasing reaction time. Nanorod growth and formation of pyramid-type morphology at both ends, *i.e.*, {111}-faceting of the nanorods, are related to the decomposition time. The decomposition time of 48 h is the period required for the development of the optimal {111}/{110} free surface ratio.

The STEM–HAADF images in Fig. 4 were taken for PTA 1/100 nanorod clusters, *i.e.* the photocatalyst, which exhibited the highest activity. From Fig. 4b, the relative arrangement of the laterally coalesced self-assembled nanorods, providing tight attachment along the {110} facets, could be observed.

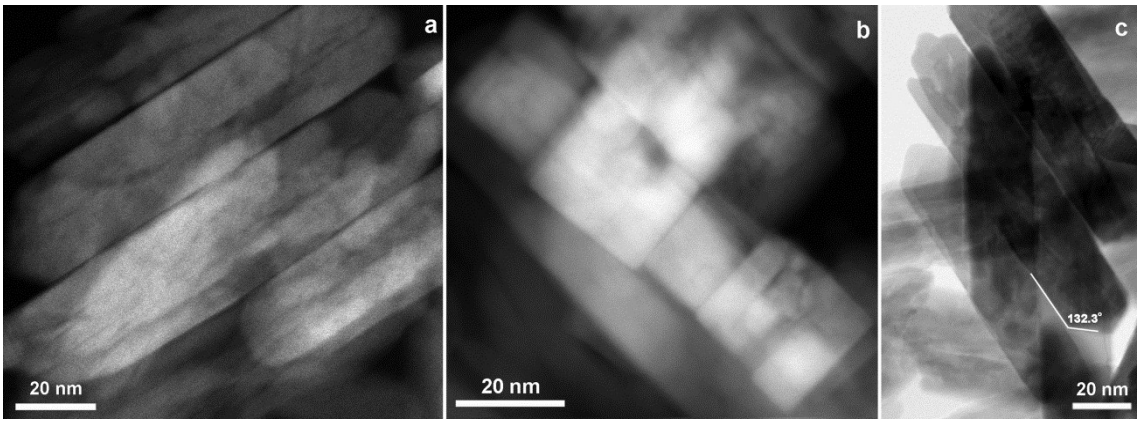

Figure 4. STEM–HAADF images of self-assembled PTA 1/100 nanorod clusters oriented with their longitudinal axes perpendicular (a), and parallel (b) to the electron beam, imaged close to the 110 and 001 zone axes, respectively; the different gray levels indicate different thickneses of

the TiO_2 nanocrystals; the bright field STEM image in (c) shows the triangular tips at both ends of the TiO_2 nanorods.

High resolution transmission electron microscopy (HRTEM) phase contrast micrographs of self-assembled PTA 1/100 nanorods is shown in Fig. 5 and TEM images of catalysts obtained at 12, 36 and 60 h of PTC thermal decomposition are presented in Fig. S6.

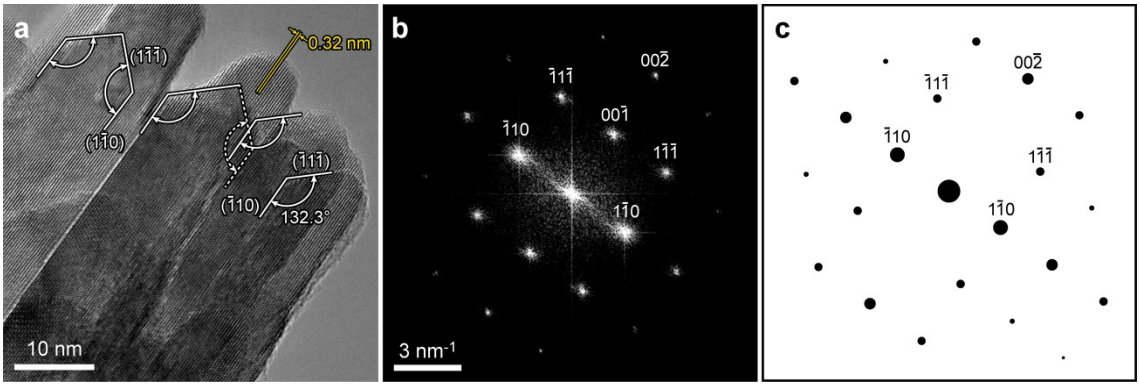

Figure 5. a) HRTEM micrograph of self-assembled PTA 1/100 nanorod clusters demonstrating orientation-dependent attachment, imaged close to the 110 zone axis (exposed {111} facets marked by arrows); b) FFT of the image in a), indicating identical orientation of all nanorods; c) simulated diffraction pattern of rutile in 110 zone axis

The preferential growth along the [001] axis of PTA 1/100 nanorods in Fig. 5a was confirmed by the fast Fourier transform (FFT) in Fig. 5b and simulated diffraction pattern in Fig. 5c, which also indicates identical orientation and an elongated habit along the *c* axis of all nanorods in Fig. 5a. In addition, self-assembled nanorods imaged close to the [110] zone axis with a large number

of {111} facets could be observed (Fig. 5a). However, it is important to keep in mind that the FFT does not rule out antisite defects at the interfaces between particles. Based on the presented results, it could be deduced that the order of the growth rate (R) of the rutile TiO_2 crystal facets is $R(001)>R(110)>R(111)$, resulting in the formation of a rectangle rod-like morphology with a four-side tapered tip.[31] The triangular tips, *i.e.*, pyramid-type morphology, of the TiO_2 nanorods are visible in Figs. 4c and 5a, showing clearly an angle of 132.3°, which corresponds to the angle between the {110} and {111} facets in a rutile crystal.[32]

The evolution of phase, crystallinity and morphology of titania obtained by controlled thermal decomposition of PTC are mainly affected by the Ti/H_2O_2 ratio and associated with the decomposition routes of PTC.[24] Quantum chemical calculations (density functional theory - DFT), provided all likely intermediate structures which helped to postulate the probable reaction mechanism (pathways) of PTC formation and decomposition (phase transformation) under different reaction conditions, *e.g.*, the Ti/H_2O_2 ratio. The optimized structure of all probable intermediate complexes (minimum of energy and frequency of each complex) obtained for defined reaction pathways, indicates that the planar placement of two peroxo groups and the stepwise formation of tri-, tetra- and penta-metallic structures favor rutile crystallization.[24]

The atomic structure near the surface of a rutile TiO_2 nanorod was imaged with high resolution transmission electron microscopy (HRTEM), shown in Fig. 6a. Several unit cells away from the surface, the bulk structure matches rutile with a [110] orientation, in agreement with our previous measurements. The atomic resolution image shows strong faceting at the surface, with a ledge structure visible. We have also observed deviations from the bulk structure, at a distance of a few unit cells from the surface. These deviations include slight lattice expansion and a changing unit cell contrast pattern at the surface. These deviations can be modeled as a stacking mismatch of

two rutile lattices along the beam direction, which causes a shift of 1/2[11$\bar{0}$] rutile unit cells on the right hand and top sides of the micrograph (near the nanorod surface). The two lattices are in registry at the lower left side of Figure 6a. An HRTEM image simulation[47] of a simple structural model is given in Fig. 6b, from a model shown in Fig. 6c. The simulated HRTEM image is in good agreement with the experimental image, indicating that this structure is a plausible explanation for the observed contrast.

This model structure results from a rutile dislocation with a line direction lying in-plane. Similar dislocation structures have been observed in past studies, for example during imperfect oriented attachment of anatase TiO_2 nanoparticles.[29,48] Here, these defects were likely introduced during the decomposition and growth process. If oriented attachment took place along the beam direction with slightly imperfect alignment between two different regions of the nanorod, the result can be lattice mismatch between these regions leading to dislocations.[29] Alternatively, dislocations with screw character can result is fast growth along the line direction.[49,50] The rutile nanorods in the present study have a high aspect ratio, which could be due to the presence of dislocations formed during growth. This possibility will be investigated in future studies.

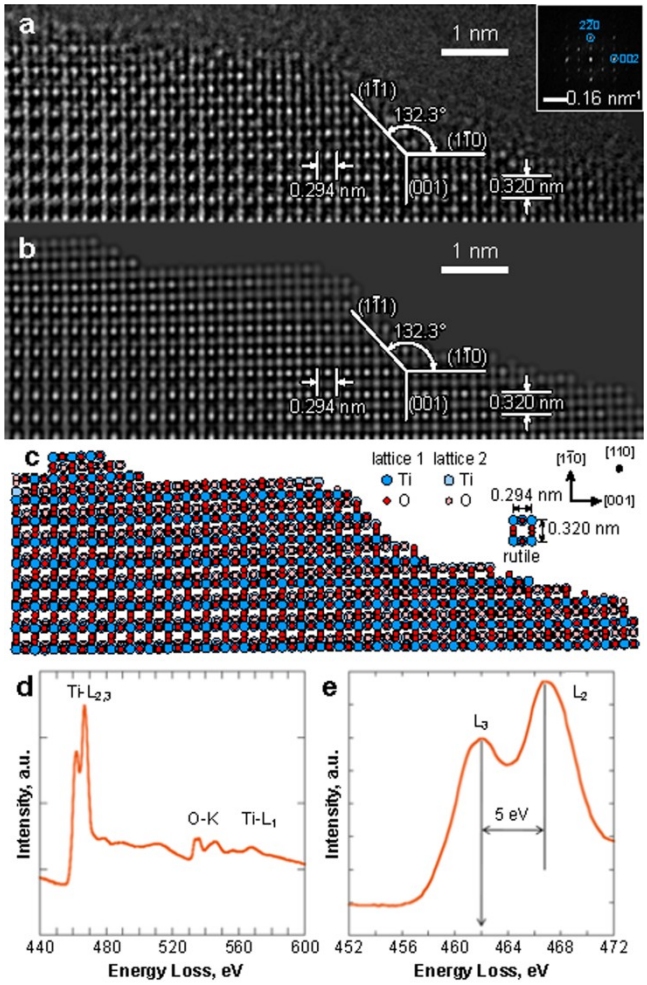

Figure 6. TEM characterization of a rutile PTA 1/100 nanorod. a) Experimental HRTEM image with inset FFT and b) a simulated HRTEM image for the atomic structure model shown in (c). (d) Ti L1 and L2,3 edges and oxygen K edge in EEL spectra of TiO_2 over energy rage of 160 eV, (e) enlarged Ti-L2,3 edge, showing L3 edge position at 462 eV, and separation between L2 and L3 edges of 5eV.

It's likely that the self-assembly of RTiO_2NRs clusters occurs *via* the oriented attachment of individual TiO_2 nanorod along the {110} facets, as observed in Figs. 4 and 5. This phenomenon is described in a recently published work,[51] in which it was demonstrated that the cluster-forming

particles underwent continuous rotation until they find a nearly perfect lattice match. Once contact has been established between adjacent nanorods, further cluster growth can proceed by nucleation and ledge growth along the [001] direction. Such processes increase the free surface ratio of {111}/{110} facets, *i.e.* they lead to significantly higher exposure of the {111} facets. This attachment process results in adjacent grains all possessing the same orientation, shown by the FFT intensity plotted in Fig 5b.

The HRTEM images shown in Figs. 6a and Fig. S7 confirm that the TiO_2 nanorod clusters are most likely formed via the mechanism of oriented attachment. Fig. 6a shows surface facets, with a slight lattice expansion at the surface. We have matched its contrast with an image simulation in Fig. 6b, for the atomic model shown in Fig 6c. This model contains a dislocation along the beam direction, which is likely a result of slight misalignment during the oriented attachment process. Fig. S7 shows additional examples of bundles of TiO_2 nanorods formed by oriented attachment, with an inset schematic showing possible growth mechanisms. Regions where TiO_2 grains have possibly joined are marked in this figure. Additionally, both Figs. 6a and S7 show ledges observed on {110} facets which indicate that ledge growth along the [001] direction likely continued occurring after attachment. The ledge growth mechanism for Rutile TiO_2 is discussed in detail in ref.[52]

Core loss EELS spectra in Fig. 6d clearly shows the presence of Ti L_3 edge at 462 eV and O K edge at 530 eV indicating pure TiO_2 nanocrystals. The Ti-L_2 edge is shifted 5 eV from the Ti-L_3 edge and it is at 467 eV (Fig. 6e). These two edges are formed by transferring $2p^{1/2}$ and $2p^{3/2}$ electrons to unoccupied orbitals, and the weak Ti-L_1 edge, hidden by the oxygen K edge, is formed by transfer of 2s electrons.[53] This confirms that Ti has valence state 4+, which is in very

good agreement with data in literature showing that L_3 line in Ti^{3+} is at 460eV and in Ti^{4+} is at 462eV.[54]

Core Level X-ray photoelectron spectroscopy (XPS) was employed in order to elucidate the oxidation state and the oxygen content on the surface of selected TiO_2 samples. Figure 7 shows the Ti 2p and O 1s core level spectra of PTA 1/100 and PTA 1/150 samples as well as from the P25 reference. All the investigated samples show similar Ti 2p spectra (Fig. 7a), characterized by the Ti^{4+} doublet components at 458.5 eV and 464.2 eV binding energies. The Ti 2p3/2 peak is symmetric and does not show any shoulder at lower binding energy due to Ti^{3+}.[55] This suggests that, within the detection limits of the XPS only Ti^{4+} ions are found on the surface of the nanorods. In the O1s spectra (Fig. 7b) four distinct components can be clearly resolved. The main oxygen component at ~529.7 eV is due to the O^{2-} species of titanium dioxide, while the one at ~530.9 eV is typically assigned to OH groups attached on TiO_2 surface.[56] The components at higher binding energies (ca. 532, 533 eV) are due to oxygen species attached to organic residuals, with possible contribution of adsorbed water molecules which appear in the same energy region. This is supported by the C 1s spectra (Figure S8) which clearly show peaks due to oxygenated carbon species. In particular the peak at 532 eV is induced by C=O species (appears at 288.8 eV in the C 1s spectrum), while the one 533.3 eV is from C–O species (appears at 286.6 eV in the C 1s spectrum). Adsorbed organic residuals are commonly observed in XPS studies of photocatalysts,[57,58] including also reports on the standard P25 material.[59] These species are formed during the TiO_2 synthesis and/or are adsorbed from the ambient environment after preparation. The XPS C 1s spectra of synthesized and reference (P25) samples shown in Fig. S8, indicate that the carbon species observed on the surface of both PTA and P25 samples are almost identical. This includes both the binding energy position and the relative intensity ratio between

the C 1s components. This is a clear demonstration that the type of adsorbed carbon species as well as, their relative population over PTA samples do not differ with those over the standard P25 reference. Consequently, if they affect the photocatalytic efficiency, then they should affect it the same way for all samples. Therefore, it is quite unlikely that the observed increase of the photocatalytic activity of PTA samples (discussed below) is induced by surface adsorbed organic residuals.

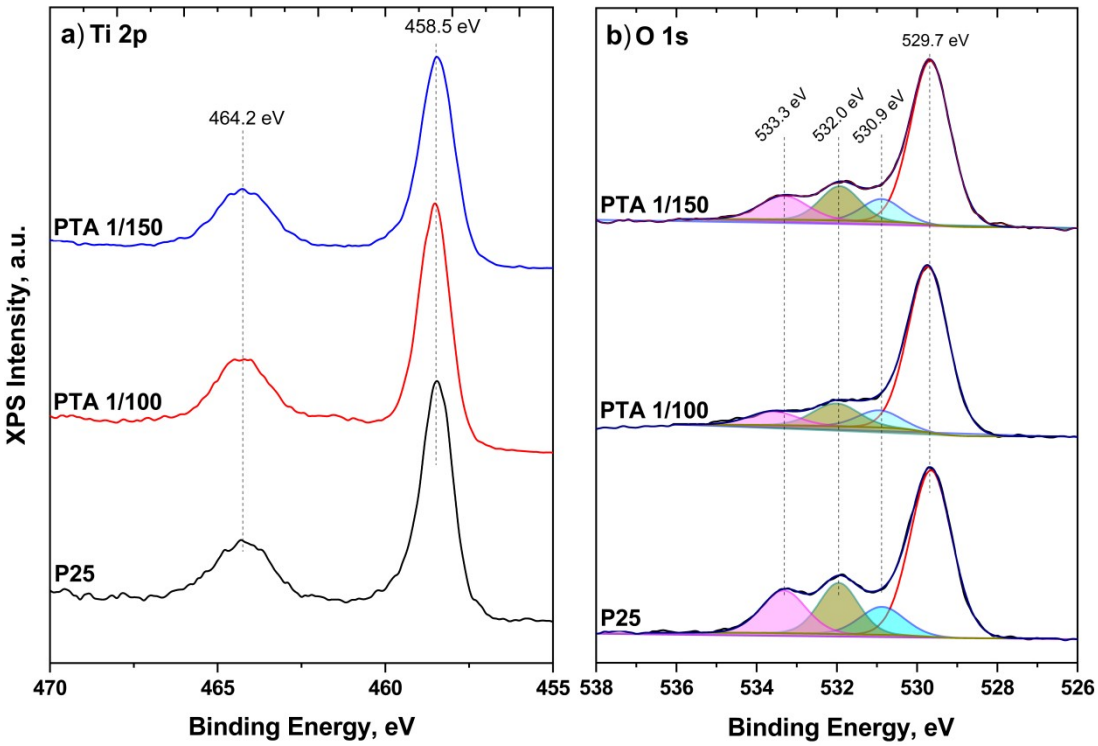

Figure 7. Ti 2p and O 1s XPS peaks collected for two selected photocatalysts, PTA 1/100 and PTA 1/150, as well as TiO_2 P25 reference material: (a) Ti 2p and (b) O 1s

Although the presence of multiple oxygen components at the O 1s spectra complicates the direct determination of O/Ti stoichiometry, the contribution of the oxygen contaminant species due to residual organics can be estimated using their intensity in the C 1s region. The O/Ti

atomic ratio calculated by the O 1s and Ti 2p spectra after subtraction of the contribution of contaminant carbon species are shown in Table 3. These results show an increase of the overall oxygenated titania species (lattice oxygen and OH groups) at PTA 1/150 and PTA 1/100 samples as compared to the reference P25. On the other hand if the O/Ti ratio is calculated considering only the O 1s component at 529.7 eV the lattice oxygen (stoichiometry of TiO_2) is the same in all samples (2.00 ± 0.04 within experimental error). This indicates that the increased $(O^{2-}+OH^-)$/Ti ratio over PTA samples, is due to the enhancement of the relative OH groups population on PTA as compared to P25 reference.

Table 3. Surface stoichiometry calculated for O 1s and Ti 2p XPS spectra* for PTA 1/100, PTA 1/150, and TiO_2 P25 reference material.

Sample	$(O^{2-}+OH^-)$/Ti
PTA150	2.28
PTA100	2.18
P25	2.11

* - Calculations were performed with the contribution of the hydroxyl species in the O 1s spectra (please refer to the deconvolution of Fig. 7b)

The analysis of the results yielded by electron paramagnetic resonance (EPR) measurements did not reveal any characteristic spectral features proving the existence of unpaired spins in our samples. This confirms that the unpaired spins or EPR active species are not present in the herein synthesized TiO_2 rutile nanorods. In particular, the EPR measurements excluded the presence of oxygen- and/or Ti^{3+} -related defects in TiO_2 nanorods.

To understand the influence of different technological parameters on photocatalytic activity of synthesized catalysts, two parameters were varied: (i) Ti/H_2O_2 molar ratio and (ii) time-

dependent PTC decomposition. The photocatalytic activity of the PTA nanorods was measured by monitoring, under UV-A illumination, the photocatalytic degradation of a common textile dye, C.I. Reactive Orange 16 (Benzema). The normalized dye concentration change *vs*. time dependences are shown in Figs. 8 and S9 and point to the fact that the herein synthesized rutile PTA nanorods reveal excellent photocatalytic activities. In particular, the Reactive Orange 16 dye was completely degraded after 20 min, 25 min and 32 min, for PTA 1/100, PTA 1/110 and PTA 150, respectively (Fig. 8). Specifically, for the PTA 1/100 photocatalysts the degradation process was completed 2.6 times faster than for the standard photocatalytic material, P25. These results show that engineering of the exposed crystal facets could contribute to enhanced photocatalytic activity. It was reported that oxidation and reduction sites on rutile particles occur on the {011} and {110} facets, respectively,[60] and are usually dominated by the more thermodynamically stable {110} facet.[61] Due to the synergistic effect between the {111} and {110} facets, rutile particles are considered to be very efficient for some photocatalytic reactions.[33] Unfortunately, reactive facets, such as {111}, have relatively higher surface energies, and smaller surface fraction at equilibrium.[32,61] The present HRTEM phase contrast and Z-contrast analyses indicate that obtained rutile nanorods were faceted by {110} lateral reductive surfaces and tapered caps on both rod ends consisting of four-side oxidative {111} facets. This is in agreement with the predicted equilibrium shape of rutile nanocrystals.[62] Additionally, due to lateral attachment along the {110} surface facets, the nanorod clusters had largely exposed oxidative {111} surface area, *i.e.* high surface ratio of {111} (oxidative)/{110} (reductive) crystal facets. The differences in the surface energy levels of TiO_2 crystal facets drives the photo-excited electrons and holes to reductive and oxidative facets, respectively, leading to their effective separation.[33] If photo-excited electrons and holes are trapped at crystallographically

different crystal facets, {110} and {111}, and subsequent surface transfer of electrons/holes (initiation of surface reaction) occurs efficiently, such mechanism would minimize possible recombination processes, which was confirmed herein by the excellent photocatalytic activity of the obtained catalysts (Fig. 8).

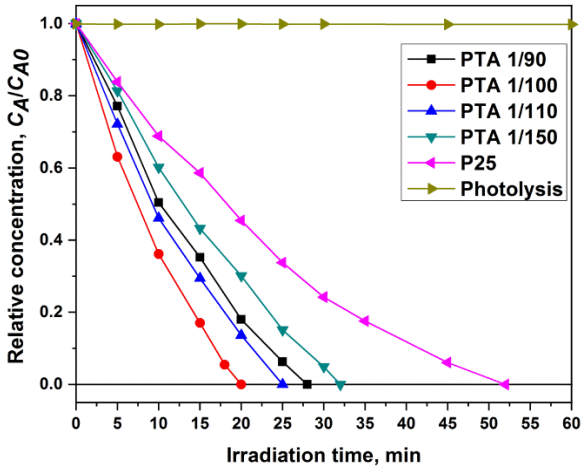

Figure 8. Relative concentration change of the C.I. Reactive Orange 16 dye *vs*. time in the presence of the photocatalysts: PTA 1/90, PTA 1/100, PTA 1/110 and PTA 1/150, and P25.

In order to obtain high photo-absorption, it is necessary to have well-dispersed photocatalyst nanoparticles, *i.e.*, the availability of surface active sites at the particle/solution interfaces. Such behavior depends on the morphology of the catalyst, *i.e.*, particle size and surface area, as well as on particle interaction. An increase in the particle size (PTA 1/150 *vs.* PTA 1/100) led to a decrease in surface area and photocatalytic activity (Fig. 8), indicating a lower availability of surface active sites due to the mass effect (larger nanorod clusters of PTA 1/150; Fig S4). Additionally, lower initial dye adsorption: 6 % for PTA 1/150, 19 % for PTA 1/110 and 24 % for

PTA 1/100 in comparison with 40 % for AEROXIDE TiO_2 P25 is an indication of the lower activity of the surface sites at the P25 catalyst. The higher degradation rate, than that of the common reference material P25, found for the well-faceted nanorod PTA 1/100 resulted from the contribution of three factors: nanoscale morphology, efficient electron excitation and electron/hole separation. Consequently, the lower electron/hole recombination rates in the well-crystallized rutile nanorods, with a high ratio of exposed oxidative/reductive crystal facets, contributed to the increased photocatalytic efficiency of this photocatalyst.

Photocatalytic efficiency is determined by the time-dependent production of the most active oxidative species (the hydroxyl radical - $OH^{\bullet}$), obtained by the reaction of holes and surface-bound water and/or hydroxyl groups,[5] the amounts of which are closely related to the degree of exposure of the {111} facet. Rutile TiO_2 microspheres with 100 % exposed {111} facets[30] showed high antibacterial activity, but no data on their photocatalytic activity was presented. The diffraction intensity ratio ($I_{(111)}/I_{(101)}$) of the microspheres[30] was lower than those of the self-assembled rutile nanorods (Table 1), indicating higher oxidative potentials of the synthesized photocatalysts. Moreover, the synthesized highly crystalline photocatalysts showed long-term stability without significant activity loss after five cycles (less than 5 %). Studies on the use of PTA photocatalysts and their modifications under UV and visible light are in progress.

CONCLUSIONS

In summary, nanocrystalline rutile TiO_2 was obtained by a low-temperature process at different Ti/H_2O_2 molar ratios and PTC thermal decomposition times. The Ti/H_2O_2 molar ratio affected the crystal size and morphology of the TiO_2 nanorod clusters obtained by lateral attachment along

{110} surface facets. In addition, preferential nanorod growth along the [001] axis, and {111} ledge growth surfaces resulted in increased amounts of oxidative {111} facets, *i.e.*, in a higher ratio of the oxidative/reductive surfaces. High photocatalytic activities of the obtained catalysts indicated that synergistic effects of the exposed crystal facets facilitate electron excitation and electron/hole separation. In adddition, the photocatlytic degradation process of a common textile dye, Reactive Orange 16, was completed 2.6 times faster in the presence of the herein synthetized PTA 1/100 than for the reference photocatalyst, P25. The presented methodology offers an alternative for the production of rutile titania with a favorable ratio of oxidative/reductive facets to obtain high photocatalytic activity and selectivity. Furthermore, our approach excludes the use of toxic capping agents and avoids the high-pressure and high-temperature treatments, thus facilitating green- and energy-efficient synthesis of nanostructured rutile TiO_2-based photocatalysts, as well as ensuring simple upscaling of the proposed technology.

EXPERIMENTAL SECTION

Materials. All materials, titanium(IV) isopropoxide (Sigma-Aldrich), H_2O_2 (30 % w/w - Merck) and 2-propanol (Merck), were used as received. Millipore deionized (DI) water (18 MΩ cm resistivity) was used for sample washing and solution preparation.

Catalysts preparation. In the present study, well-defined nano-sized rutile TiO_2 photocatalysts were prepared by low-temperature thermal decomposition (without hydrothermal treatment) of the peroxo titanium complex (PTC), using a significantly higher Ti/H_2O_2 molar ratio than recently presented in the literature.[24] In a three-necked flask (50 mL) immersed in an ice water bath and equipped with a condenser, dropping funnel and thermometer, 11 mL of deionized water was added under magnetic stirring. In a

typical reaction, an alcoholic solution of Ti(IV) isopropoxide (1.65 mmol in 5.6 mL 2-propanol) was slowly added to the cold water (0-5 °C) under vigorous stirring, whereby a turbid white dispersion was obtained. After cooling to 0 °C, an appropriate amount of 30 % H_2O_2 solution (molar ratio of Ti/H_2O_2: 1/90, 1/100, 1/110 and 1/150) was added drop-wise keeping the temperature constant. The turbid white dispersion gradually changed to an orange-yellowish clear solution indicating the formation of water-soluble PTC. At this moment, the ice-bath was removed and mixing was continued for an additional 30 min until the sample reached room temperature. The flask was then immersed in an oil bath and subjected to heating at 97 °C for 12, 24, 36, 48 or 60 h. After completion of the reaction, the obtained TiO_2 dispersion was filtered (0.05 μm pore size polytetrafluoroethylene filter membrane), washed with deionized water, dried at 70 °C for 24 h, and ground to a fine powder.

Characterization. Fourier-transform infrared (FTIR) spectra were recorded in the transmission mode using a BOMEM (Hartmann&Braun) spectrometer. The crystal structure of the as-prepared titania was characterized by X-ray diffraction (XRD) analysis using a BRUKER D8 ADVANCE with Vario 1 focusing primary monochromator ($CuK_{\alpha 1}$ radiation, λ = 1.54059 Å). The simulated XRD pattern of rutile TiO_2 with a random crystallite orientation (PTA Simul) was performed using the FindIt software package. The textural parameters of the obtained TiO_2 powders were examined using the BET (Brunauer-Emmett-Teller) method for the determination of the specific surface area, the BJH (Barrett-Joyner-Halenda) method for the determination of the mesoporosity parameters and the Gurvich method for quantification of the total pore volume based on nitrogen adsorption and desorption data at liquid nitrogen temperature (ASAP 2020, Micromeritics - USA). The optical properties of the obtained photocatalysts were characterized using diffuse reflectance spectroscopy (DRS). The DRS spectra were collected in the wavelength range from 220 to 1000 nm using a Shimadzu 2600 UV-Vis spectrophotometer equipped with an integrating sphere, using barium sulfate as a standard. Morphological characterization was performed using a field-emission gun scanning electron microscope (FEG-SEM) MIRA3 XMU (TESCAN, Czech

Republic). Conventional transmission electron microscopy (CTEM) was performed using AEM JEOL 200CX and JEOL 2100F microscopes at 200 kV. High resolution transmission electron microscopy (HRTEM) and spectroscopy analysis were realized using the TEAM0.5 aberration-corrected transmission electron microscope, equipped with GIF Tridiem imaging filter. The CrystalKitX and MacTempas software packages were used for structure modeling and image simulation of the experimental high resolution transmission electron microscopy data, as well as custom Matlab routines.

Electron Paramagnetic Resonance (EPR) spectra of TiO_2 nanorods were recorded on a Varian E109 EPR spectrometer equipped with a Model 102 Microwave bridge. The sample temperature was maintained between 15-40 K, using an Air Products LTR liquid helium cryostat. The samples were frozen at 77 K prior to the EPR measurements. The microwave frequency of 9.25 GHz was used while the scans were measured at the magnetic field range of 862 G to 4138 G at a microwave power of 2 mW and 20 μW. The spectra were acquired at a modulation frequency of 100 kHz with a modulation amplitude of 3.2 G.

The X-ray photoelectron spectroscopy (*XPS*) measurements were carried out in an ultrahigh vacuum (UHV) setup equipped with a 150 nm VSW Class WA hemispherical electron analyzer. A monochromatized Al Ka X-ray source (1486.6 eV; anode operating at 240 W) was used for XPS. The binding energy scale was corrected by the C 1s peak of adventitious carbon at 285 eV as an internal reference. All samples showed similar electrostatic charging magnitude (0.8 to 0.9 eV).

Photocatalytic activity. Photocatalytic decomposition of the textile dye, C.I. Reactive Orange 16 (Benzema), was followed by optical absorption spectroscopy changes in the presence of the catalyst. Typically, 25 mg of photocatalyst was added in 12.5 ml of aqueous dye solution (50 mg L^{-1}) in a Pyrex glass photoreactor at constant temperature (293 K) under water cooling. Prior to irradiation, the mixture was ultrasonicated in a water bath for 5 min to ensure good dispersion of the photocatalysts. Subsequently, the mixture was stirred in the dark for 30 min in order to establish adsorption/desorption equilibrium between dye molecules and the surface of the photocatalysts. The mixture was then

illuminated with a UV-A lamp (125 W; 12.7 mW cm^{-2}; Philips) under magnetic stirring. A 1.0 mL aliquot of the suspension (after partial settling) was drawn out and separated from the photocatalysts by filtration using a 0.2 μm poly(vinylidene fluoride) syringe filter (Whatman). The time-dependent dye concentration change was followed by the absorbance decrease using a Shimadzu 1800 UV–Vis spectrophotometer. After each sampling and absorbance measurement, the filtrate was returned to the photoreactor. The UV light irradiation intensity was measured by a UVX Digital Ultraviolet Intensity Meter (Cole-Parmer, USA; Model: 97-0015-02 (UVX)) using a 365 nm sensor (97-0016-02(UVX36)). Comparative experiments were performed using a commercial AEROXIDE TiO_2 P25 Degussa (Evonik) photocatalyst.

■ ASSOCIATED CONTENT

The Supporting Information is available free of charge on the ACS Publications website. Additional experimental results: Figures S1–S9, Tables S1–S3, and supplementary references.

■ AUTHOR INFORMATION

Corresponding Authors

*E-mail: Veljko R. Djokic: **vdjokic@tmf.bg.ac.rs**

*E-mail: Velimir R. Radmilovic: **vrradmilovic@tmf.bg.ac.rs**

*E-mail: Djordje T. Janackovic: **nht@tmf.bg.ac.rs**

■ ACKNOWLEDGMENTS

Financial support through the Ministry of Education, Science and Technological Development of the Republic of Serbia, Contract No. 451-03-68/2020-14/200135, is acknowledged. The

authors thank Ileana Florea from IPCMS, of Strasbourg for performing part of the STEM analysis and Mireille Richard from IMN of Nantes for fruitful discussions. V.R. Radmilović acknowledges support from the Serbian Academy of Sciences and Arts under project No. F-141. We thank Dr. Junko Yano for permission to use the EPR Lab at Lawrence Berkeley National Lab, and Dr. Ruchira Chatterjee for measuring EPR spectra of TiO_2 nanorods. Work at the Molecular Foundry was supported by the Office of Science, Office of Basic Energy Sciences, of the U.S. Department of Energy under Contract No. DE-AC02-05CH11231.

TABLE OF CONTENTS GRAPHIC

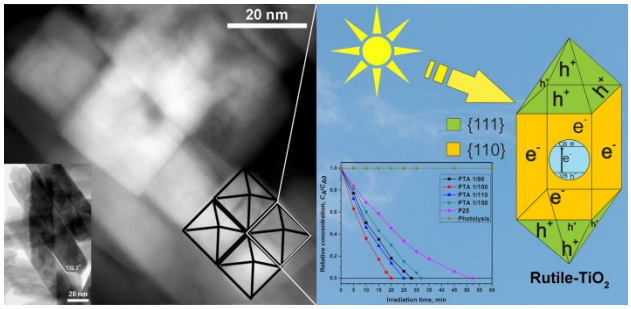

REFERENCES

[1] Fujishima, A.; Zhang, X.; Tryk, D. A. TiO_2 Photocatalysis and Related Surface Phenomena. *Surf. Sci. Rep*. **2008**, 63, 515–582.

[2] Fujishima, A.; Honda, K. Electrochemical Photolysis of Water at a Semiconductor Electrode. *Nature* **1972**, 238, 37-38.

[3] Henderson, M. A. A Surface Science Perspective on TiO_2 Photocatalysis. *Surf. Sci. Rep.* **2011**, 66, 185–297.

[8] Chen, X.; Mao, S. S. Titanium Dioxide Nanomaterials: Synthesis, Properties, Modifications, and Applications. *Chem. Rev.* **2007**, 107, 2891–2959.

[9] Byrnea, C.; Subramanian, G.; Pillai, S. C. Recent Advances in Photocatalysis for Environmental Applications. *Environ. Chem. Eng*. **2018**, 6, 3531–3555.

[10] Guo, Q.; Zhou, C.; Ma, Z.; and Yang, X. Fundamentals of TiO_2 Photocatalysis: Concepts, Mechanisms, and Challenges. *Adv. Mater.* **2019**, 31, 1901997.

[11] Ziental, D.; Czarczynska-Goslinska, B.; Mlynarczyk, D. T.; Glowacka-Sobotta, A.; Stanisz, B.; Goslinski, T.; and Sobotta, L. Titanium Dioxide Nanoparticles: Prospects and Applications in Medicine. *Nanomaterials*, **2020**, 10, 387.

[12] Rodríguez-González, V.; Terashima, C.; Fujishima, A. Photocatalysis Applications of photocatalytic titanium dioxide-based nanomaterials in sustainable agriculture. *J. Photochem. Photobiol. C* **2019**, 40, 49–67.

[13] Marchand, R., Brohan, L., Tournoux, M. TiO_2(B) a New Form of Titanium Dioxide and the Potassium Octatitanate $K_2Ti_8O_{17}$. *Mat. Res. Bull.,* **1980**, 15, 1129-1133.

[14] Feist, T. P., Davies, P. K. The Soft Chemical Synthesis of TiO_2(B) from Layered Titanates. ***J.*** *Solid State Chem*., **1992**, 101, 275-295.

[15] Cassaignon, S.; Koelsch, M.; Jolivet, J.-P. From $TiCl_3$ to TiO_2 Nanoparticles (Anatase, Brookite and Rutile): Thermohydrolysis and Oxidation in Aqueous Medium. *J. Phys. Chem. Solids* **2007**, 68, 695–700.

[16] Linsebigler, A. L.; Lu, G. Q.; Yates, J. T. Photocatalysis on TiO_2 Surfaces: Principles, Mechanisms, and Selected Results. *Chem. Rev*. **1995**, 95, 735–758.

[18] Zhang, Y.; Wu, L.; Zeng, Q.; Zhi, J. Synthesis and Characterization of Rutile TiO_2 Nano-Ellipsoid by Water-Soluble Peroxotitanium Complex Precursor. *Mater. Chem. Phys.* **2010**, 121,

235–240.

[19] Yin, H.; Wada, Y.; Kiatamura, T.; Kambe, S.; Murasawa, S.; Mori, H.; Sakata T.; Yanagida, S. Hydrothermal Synthesis of Nanosized Anatase and Rutile TiO_2 Using Amorphous Phase TiO_2. *J. Mater. Chem.* **2001**, 11, 1694–1703.

[20] Watson, S. S.; Beydoun, D.; Scott, J. A.; Amal, R. The Effect of Preparation Method on the Photoactivity of Crystalline Titanium Dioxide Particles. *Chem. Eng. J.*, **2003,** 95, 213–220.

[21] Murakami, N.; Kurihara, Y.; Tsubota, T.; Ohno, T. Shape-Controlled Anatase Titanium(IV) Oxide Particles Prepared by Hydrothermal Treatment of Peroxo Titanic Acid in the Presence of Polyvinyl Alcohol. *J. Phys. Chem.* **2009,** 113, 3062–3069.

[24] Nag, M.; Ghosh, S.; Rana, R.K.; Manorama, S. V. Controlling Phase, Crystallinity, and Morphology of Titania Nanoparticles with Peroxotitanium Complex: Experimental and Theoretical Insights. *J. Phys. Chem. Lett.* **2010,** 1, 2881–2885.

[25] Penn, R. L.; Banfield, J. F. Morphology Development and Crystal Growth in Nanocrystalline Aggregates under Hydrothermal Conditions: Insights from Titania. *Geochim. Cosmochim. Acta*, **1999,** 63, 1549–1557.

[26] Testino, A.; Bellobono, I.R.; Buscaglia, V.; Canevali, C.; D'Arienzo, M.; Polizzi, S.; Scotti, R.; Morazzoni, F. Optimizing the Photocatalytic Properties of Hydrothermal TiO_2 by the Control of Phase Composition and Particle Morphology. A Systematic Approach. *J. Am. Chem. Soc.* **2007,** 129, 3564–3575.

[27] Scotti, R.; Bellobono, I.R.; Canevali, C.; Cannas, C.; Catti, M.; D'Arienzo, M.; Musinu, A.; Polizzi, S.; Sommariva, M.; Testino, A.; Morazzoni, F. Sol–Gel Pure and Mixed-Phase Titanium Dioxide for Photocatalytic Purposes: Relations between Phase Composition, Catalytic Activity, and Charge-Trapped Sites. *Chem. Mater.* **2008,** 20, 4051–4061.

[28] Jung, H. S.; Kim, H. Origin of Low Photocatalytic Activity of Rutile TiO_2. *Electron. Mater. Lett.* **2009,** 5, 73–76.

[29] Penn, R. L.; Banfield, J.F. Imperfect Oriented Attachment: Dislocation Generation in Defect-Free Nanocrystals. *Science* **1998,** 281, 969–971.

[30] Sun, L.; Qin, Y.; Cao, Q.; Hu, B.; Huang, Z.; Ye, L.; Tang, X. Novel Photocatalytic Antibacterial Activity of TiO_2 Microspheres Exposing 100% Reactive {111} Facets. *Chem. Commun.*, **2011,** 47, 12628–12630.

[31] Huang, X.; Pan, C. Large-Scale Synthesis of Single-Crystalline Rutile TiO_2 Nanorods via a One-Step Solution Route. *J. Cryst. Growth*, **2007**, 306, 117–122.

[32] Kakiuchi, K.; Hosono, E.; Imai, H.; Kimura, T.; Fujihara, S. {1 1 1}-Faceting of Low-Temperature Processed Rutile TiO_2 Rods. *J. Cryst. Growth*, **2006**, 293, 541–545.

[33] Bae, E.; Murakami, N.; Ohno, T. Exposed Crystal Surface-Controlled TiO_2 Nanorods Having Rutile Phase from $TiCl_3$ under Hydrothermal Conditions. *J. Mol. Catal. A: Chem.* **2009,** 300, 72–79.

[34] Zhuangchai, L., Feng, P., Hongjuan, W., Hao, Y., Shanqing, Z. and Huijun, Z. A New Insight Into Regulating High Energy Facets of Rutile TiO_2. *J. Mater. Chem. A*, **2013**, 1, 4182-4185.

[35] Pang, C.L.; Thorton, G. The Many Faces of Rutile Titania. *Surf, Sci.* **2006,** 600, 4405–4406.

[36] Hosono, E.; Fujihara, S.; Kakiuchi, K.; Imai, H. Growth of Submicrometer-Scale Rectangular Parallelepiped Rutile TiO_2 Films in Aqueous $TiCl_3$ Solutions under Hydrothermal Conditions. *J. Am. Chem. Soc.* **2004**, 126, 7790–7791.

[37] Reyes-Coronado, D.; Rodríguez-Gattorno, G.; Espinosa-Pesqueira, M. E.; Cab, C.; de Coss, R.; Oskam, G. Phase-Pure TiO_2 Nanoparticles: Anatase, Brookite and Rutile. *Nanotechnology* **2008,** 19, 145605 (10pp).

[38] Li, Y.; Pera-Titus, M.; Xiong, G.; Yang, W.; Landrivon, E.; Miachon, S.; Dalmon, J.-A. Nanocomposite MFI-Alumina Membranes via Pore-Plugging Synthesis: Genesis of the Zeolite Material. *J. Membr. Sci.* **2008,** 325, 973–981.

[39] Stengl, V.; Bakardjieva, S.; Murafa, N.; Houskova, V.; Lang, K. Visible-Light Photocatalytic Activity of TiO_2/ZnS Nanocomposites Prepared by Homogeneous Hydrolysis. *Microporous*

Mesoporous Mater. **2008**, 110, 370–378.

[40] Yan, J.; Wu, G.; Guan, N.; Li, L.; Li, Z. and Cao, X. Understanding the effect of surface/bulk defects on the photocatalytic activity of TiO_2: anatase versus rutile. *Phys.Chem. Chem. Phys.* **2013**, 15, 10978--10988.

[41] Li, J. G.; Ishigaki, T.; and Sun, X. Anatase, Brookite, and Rutile Nanocrystals via Redox Reactions under Mild Hydrothermal Conditions: Phase-Selective Synthesis and Physicochemical Properties. *J. Phys. Chem. C* **2007**, 111, 4969-4976.

[42] Ohtani, B.; Prieto-Mahaney, O. O.; Li, D.; Abe, R. What is Degussa (Evonik) P25? Crystalline composition analysis, reconstruction from isolated pure particles and photocatalytic activity test. *J. Photochem. Photobiol. A*. **2010**, 216, 179–182.

[43] Cha, S. I.; Hwang, K. H.; Kim, Y. H.; Yun, M. J.; Seo, S. H.; Shin, Y. J.; Moon, J. H.; and Lee, D. Y. Crystal splitting and enhanced photocatalytic behavior of TiO_2 rutile nano-belts induced by dislocations. *Nanoscale* **2013**, 5, 753–758.

[44] Maras, E.; Saito, M.; Inoue, K.; Jónsson, H.; Ikuhara, Y.; McKenna, K. P. Determination of the structure and properties of an edge dislocation in rutile TiO_2. *Acta Materialia* **2019**, 163, 199-207.

[45] Diebold, U. The Surface Science of Titanium Dioxide. *Surf. Sci. Rep.* **2003**, 48, 53–229.

[46] Etacheri, V.; Seery, M. K.; Hinder, S. J.; and Pillai, S. C. Oxygen Rich Titania: A Dopant Free, High Temperature Stable, and Visible-Light Active Anatase Photocatalyst. *Adv. Funct. Mater.* **2011**, 21, 3744–3752.

[47] Kirkland, E.J. *Advanced Computing in Electron Microscopy*, 2nd Edition, Springer Science and Business Media: New York, **2010**.

[48] Zhang, H.; De Yoreo, J.J.; and Banfield, J.F. A Unified Description of Attachment-Based Crystal Growth. *ACS Nano* **2014**, 8, 6526-6530.

[49] Frank, F.C. The Influence of Dislocations on Crystal Growth. *Discuss. Faraday Soc.* **1949**, 5, 48-54.

[50] Bierman, M.J.; Lau, Y.K.A.; Kvit, A.V.; Schmitt, A.L.; and Jin, S. Dislocation-Driven Nanowire Growth and Eshelby Twist. *Science* **2008**, 320, 1060-1063.

[51] Li, D.; Nielsen, M. H.; Lee, J. R. I.; Frandsen, C.; Banfield, J. F.; De Yoreo, J. J. Direction-Specific Interactions Control Crystal Growth by Oriented Attachment. *Science* **2012**, 336, 1014–

1018.

[52] Lin, J.; Heo, Y. U.; Nattestad, A.; Sun, Z.; Wang, L.; Jung, H. K.; & Dou, S. X. 3D Hierarchical Rutile TiO_2 and Metal-free Organic Sensitizer Producing Dye-sensitized Solar Cells 8.6% Conversion Efficiency. *Sci. Rep.* **2015**, 4, 5769.

[53] Leapman, R.D.; Grunesand, L.A.; Fejes, P.L. Study of the L_{23} Edges in the 3*d* Transition Metals and Their Oxides by Electron-Energy-Loss Spectroscopy with Comparisons to Theory. *Phys. Rev. B* **1982,** 26, 614-635.

[54] Otten, M.T.; Miner, B.; Rask, J.H. and Buseck, P.R. The Determination of Ti, Mn and Fe Oxidation States in Minerals by Electron Energy-Loss Spectroscopy. *Ultramicroscopy* **1985,** 18, 285-290.

[55] Papaefthimiou, V.; Dintzer, T.; Lebedeva, M.; Teschner, D.; Hävecker, M.; Knop-Gericke, A.; Schlögl, R.; Pierron-Bohnes, V.; Savinova, E.; and Zafeiratos, S. Probing Metal–Support Interaction in Reactive Environments: An in Situ Study of PtCo Bimetallic Nanoparticles Supported on TiO_2. *J. Phys. Chem. C* **2012**, 116 (27), 14342−14349

[56] McCafferty, E. and Wightman, J. P. Determination of the Concentration of Surface Hydroxyl Groups on Metal Oxide Films by a Quantitative XPS Method. *Surf. Interface Anal.* **1998**, 26**,** 549–564.

[57] Lu, Z.; Zeng, L.; Song, W.; Qin, Z.; Zeng, D.; Xie, C. In situ synthesis of C-TiO_2/g-C_3N_4 heterojunction nanocomposite as highly visible light active photocatalyst originated from effective interfacial charge transfer. *Appl. Catal. B.* **2017**, 202, 489–499.

[58] Ren, W.; Ai, Z.; Jia, F.; Zhang, L.; Fan, X.; Zou, Z. Low temperature preparation and visible light photocatalytic activity of mesoporous carbon-doped crystalline TiO_2. *Appl. Catal. B.* **2007**, 69, 138–144.

[59] Bessergenev, V.G.; Mateus, M.C.; Botelho do Rego, A.M.; Hantusch, M.; Burkel, E. An improvement of photocatalytic activity of TiO_2 Degussa P25 powder. *Applied Catalysis A: General* **2015**, 500, 40–50.

[60] Ohno, T.; Sarukawa, K.; Matsumara, M. Crystal Faces of Rutile and Anatase TiO_2 Particles and Their Roles in Photocatalytic Reactions. *New J. Chem.* **2002**, 26, 1167–1170.

[61] Oliver, P. M.; Watson, G. W.; Kelsey, E. T.; Parker, S. C. Atomistic Simulation of the Surface Structure of the TiO_2 Polymorphs Rutile and Anatase. *J. Mater. Chem.* **1997**, 7(3), 563–568.

[62] Liu, G.; Yu, J. C.; Lu, G. Q. (M.); Cheng, H.-M. Crystal Facet Engineering of Semiconductor Photocatalysts: Motivations, Advances and Unique Properties. *Chem. Commun.* **2011,** 47, 6763–6783.